Journal of Computational Physics 350 (2017) 891–906

Contents lists available at ScienceDirect

Journal of Computational Physics

www.elsevier.com/locate/jcp

A fully-implicit Particle-In-Cell Monte Carlo Collision code for the simulation of inductively coupled plasmas

S. Mattei [a,b,*], K. Nishida [c], M. Onai [c], J. Lettry [a], M.Q. Tran [b], A. Hatayama [c]

[a] CERN, CH-1211 Geneva 23, Switzerland
[b] Swiss Plasma Center, EPFL, Station 13, CH-1015 Lausanne, Switzerland
[c] Faculty of Science and Technology, Keio University, 3-14-1 Hiyoshi, Kohoku-ku, Yokohama 223-8522, Japan

ARTICLE INFO

Article history:
Received 10 January 2017
Received in revised form 30 June 2017
Accepted 9 September 2017
Available online 12 September 2017

Keywords:
Particle-In-Cell
Monte Carlo collision
Implicit
Inductively coupled plasmas

ABSTRACT

We present a fully-implicit electromagnetic Particle-In-Cell Monte Carlo collision code, called NINJA, written for the simulation of inductively coupled plasmas. NINJA employs a kinetic enslaved Jacobian-Free Newton Krylov method to solve self-consistently the interaction between the electromagnetic field generated by the radio-frequency coil and the plasma response. The simulated plasma includes a kinetic description of charged and neutral species as well as the collision processes between them. The algorithm allows simulations with cell sizes much larger than the Debye length and time steps in excess of the Courant–Friedrichs–Lewy condition whilst preserving the conservation of the total energy. The code is applied to the simulation of the plasma discharge of the Linac4 H^- ion source at CERN. Simulation results of plasma density, temperature and EEDF are discussed and compared with optical emission spectroscopy measurements. A systematic study of the energy conservation as a function of the numerical parameters is presented.

1. Introduction

In recent years there has been a strong interest in applications based on Inductively Coupled Plasmas (ICP): large-area integrated circuit manufacturing [1], medical devices [2], ion sources for accelerators [3] and fusion [4]. Key features of ICP driven discharges are the capability of obtaining high density plasmas (10^{17}–10^{18} m^{-3}) even at low gas pressures, and to operate without direct contact of the electrodes with the plasma. Modern applications set demanding specifications on the design and operation of ICP discharges, making it essential to develop detailed plasma models to gain insights into the underlying physics.

Theoretical and experimental studies have highlighted the importance of kinetic effects in ICPs [5–7] as well as local and non-local kinetics [8]. Modeling work of ICPs has mainly been performed using fluid [9,10] and hybrid codes [11,12], while only few papers can be found on kinetic modeling that are particularly targeted at the low-density regime [13–15]. This is partially because kinetic simulations of high density, low temperature plasmas require very large computational resources and remained intractable for many years. One of the techniques to simulate plasmas from a kinetic point of view is the Particle-In-Cell (PIC) algorithm [16]. In its classical implementation, the time dependent governing equations are solved with an explicit leap-frog integration scheme. While this technique is simple and second order accurate, its limitations arise from the stringent time step Δt and cell size Δx required for its stability. In fact Δt must be kept sufficiently small

* Corresponding author at: CERN, CH-1211 Geneva 23, Switzerland.
E-mail address: stefano.mattei@cern.ch (S. Mattei).

http://dx.doi.org/10.1016/j.jcp.2017.09.015

to resolve the fastest wave propagations, typically electromagnetic radiation or plasma oscillations (Langmuir waves), in order to satisfy the Courant–Friedrichs–Lewy condition [16]. Δx on the other hand must resolve the finest electron scales happening at the Debye length λ_{De} to avoid a numerical plasma heating known in the literature as finite-grid instability [17]. This is a strong limitation for the simulation of ICPs, as λ_{De} can be in the order of tens of μm, while the typical plasma chamber size is several centimeters large, leading to a considerable number of cells to be simulated.

To overcome these limitations, alternative PIC implementations using implicit integration schemes have been considered since the 80's, starting with the pioneering work of Mason [18] and Denavit [19]. Implicit PICs require the concurrent solution of the non-linear coupling of the field equations with the particles' equations of motion and originally, due to the complexity of the problem, a number of semi-implicit codes were first developed (implicit moment [18,19] and direct implicit [20]). Recently, thanks to advances in computing and numerical techniques, the fully-implicit solutions to the non-linear field-particles problem has been successfully addressed [21,22]. These algorithms are shown to be unconditionally stable for any choice of Δt and replace the constraint on Δx to resolve λ_{De} by a much more relaxed condition that particles should not cross more that one cell in one time step. This is a significant improvement over explicit codes because the choices of Δt and Δx are no longer bound to strict stability requirements, but can be chosen to resolve only the scales of interest in the plasma under investigation.

Based on these considerations, we have developed a fully-implicit electromagnetic PIC code, called NINJA, for the kinetic simulation of ICPs. Our motivation originated from the investigation of the Linac4 H^- ion source at CERN [3], whose plasma is created in an ICP in cylindrical configuration. NINJA is a 2.5D PIC in cylindrical coordinates, where the electromagnetic (EM) fields are solved in 2D assuming azimuthal symmetry ($\partial/\partial\theta = 0$), while the particles' motion is solved in 3D3V. The model is supplemented with a Monte Carlo Collision (MCC) algorithm to describe the plasma chemistry as well as a neutral transport module including atomic and molecular (vibrationally resolved) particle tracking for hydrogen. This study represents, in our best knowledge, the first application of a fully-implicit algorithm for the simulation of bounded, collisional plasmas, including the coupling with a Monte Carlo Collision module. This extends the previous work on the fully-implicit algorithm for unbounded, collision-less plasmas described in [21,22]. We present a description of the algorithms, their implementation, a performance analysis, a comparison to analytic solutions and the application of the code to the investigation of the hydrogen discharge in the Linac4 H^- ion source.

2. Method

2.1. Governing equations

The goal of our simulations is to describe the plasma dynamics in an ICP. This requires modeling the interaction between the EM field generated by the Radio-Frequency (RF) coil and the corresponding plasma response, composed of the particles' motion and the collision processes between them. We are interested in describing the high density regime of an ICP, in which the coupling between the coil and the plasma is of the inductive type (H-mode) [23]. The electric field $\mathbf{E}$ and magnetic field $\mathbf{B}$ are given by Maxwell's equations in which the current density $\mathbf{J}$ is the sum of the plasma $\mathbf{J}_{pl}$ and the RF coil $\mathbf{J}_{RF}$ contributions:

$$\nabla \cdot \mathbf{E} = \frac{\rho}{\epsilon_0} \tag{1}$$

$$\nabla \cdot \mathbf{B} = 0 \tag{2}$$

$$\frac{\partial \mathbf{B}}{\partial t} = -\nabla \times \mathbf{E} \tag{3}$$

$$\frac{\partial \mathbf{E}}{\partial t} = \frac{1}{\epsilon_0 \mu_0} \nabla \times \mathbf{B} - \frac{1}{\epsilon_0} \mathbf{J} \qquad \mathbf{J} = \mathbf{J}_{RF} + \mathbf{J}_{pl} \tag{4}$$

with t representing time, ρ the charge density and ϵ_0, μ_0 the permittivity and permeability of free space respectively.

While $\mathbf{J}_{RF}$ is externally imposed, the plasma contribution $\mathbf{J}_{pl}$ results from the motion of the charged particles in the plasma. Kinetically this is represented by the first moment of the distribution function f_s (normalized to the plasma density n_s) of each plasma species s (e.g. electron, ion), resulting in:

$$\mathbf{J}_{pl} = \sum_s q_s \int_V \mathbf{v} f_s(\mathbf{x}, \mathbf{v}, t) dv \tag{5}$$

with $\mathbf{x}$ the position, $\mathbf{v}$ the velocity and q_s the electric charge of the species s. The particles' position $\mathbf{x}_p$ and velocity $\mathbf{v}_p$ define the distribution function f_s, and are mathematically described by Newton's equations of motion:

$$\frac{d\mathbf{x}_p}{dt} = \mathbf{v}_p \tag{6}$$

$$m_s \frac{d\mathbf{v}_p}{dt} = q_s(\mathbf{E}_p + \mathbf{v}_p \times \mathbf{B}_p) + \mathbf{F}_c \tag{7}$$

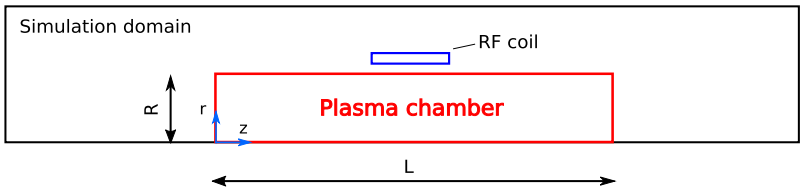

Fig. 1. Typical simulation domain: the plasma chamber is a cylinder of radius R and length L, while the calculation of the electromagnetic fields is performed on a larger domain. The RF coil is modeled as a perfect conductor with rectangular cross-section and given input current.

where m_s is the mass of the particle species s; $\mathbf{E}_p, \mathbf{B}_p$ represent the EM field acting on the particle p and $\mathbf{F}_c$ is the collisional force. Similarly, the motion of the neutral particles is described by equations (6), (7) with $q_s = 0$. The self-consistent solution of the field equations (1), (2), (3), (4) and Newton's equations of motion (6), (7), non-linearly coupled via equation (5) represent the full system of equations to be solved.

The governing equations are solved on a domain similar to the one represented in Fig. 1: the plasma chamber is a cylinder of radius R and length L while the calculation of the electromagnetic fields is performed on a larger domain in order to include the coil and to avoid large EM reflections at the boundary. The coil is modeled as a perfect conductor, with rectangular cross-sectional area and a given input $\mathbf{J}_{RF}$. Our model is developed in cylindrical coordinates. Given the azimuthal symmetry of this configuration we assume that the EM field is independent of the azimuthal coordinate ($\partial/\partial\theta = 0$), while the particle motion is fully 3D3V.

2.2. PIC scheme

We solve the governing equations using an implicit θ-scheme time integration and central differences on a Yee cell [24] for the spatial discretization (standard and not explicitly indicated). The time-discretized Maxwell's equations become:

$$\frac{\mathbf{B}^{n+1} - \mathbf{B}^n}{\Delta t} = -\nabla \times \mathbf{E}^{n+\theta} \tag{8}$$

$$\frac{\mathbf{E}^{n+1} - \mathbf{E}^n}{\Delta t} = \frac{1}{\epsilon_0 \mu_0} \nabla \times \mathbf{B}^{n+\theta} - \frac{1}{\epsilon_0} \mathbf{J}^{n+\frac{1}{2}} \tag{9}$$

where the superscript indicates time in units of Δt, and the fields on the right hand side are evaluated as a weighted average between the current time step n and the new one $n+1$:

$$X^{n+\theta} = \theta X^{n+1} + (1-\theta) X^n \tag{10}$$

The parameter θ affects the energy conservation and must be chosen $0.5 \leq \theta \leq 1$ else the scheme is divergent, while $\mathbf{J}$ is weighted at the half time step to avoid unphysical plasma heating/cooling [25]. The two divergence equations (1), (2) are not explicitly solved as equation (1) is automatically satisfied as long as charge conservation holds while equation (2) is always valid if satisfied initially [16].

The particles' equations of motion are first solved in the PIC scheme in their collision-less form, the inclusion of the collision operator is shown in section 2.5. Equations (6), (7) are discretized as follows:

$$\frac{\mathbf{x}^{n+1} - \mathbf{x}^n}{\Delta t} = \mathbf{v}_p^{n+\frac{1}{2}} \tag{11}$$

$$\frac{\mathbf{v}^{n+1} - \mathbf{v}^n}{\Delta t} = \frac{q_s}{m_s} (\mathbf{E}_p^{n+\theta} + \mathbf{v}_p^{n+\frac{1}{2}} \times \mathbf{B}_p^{n+\theta}) \tag{12}$$

The fields $\mathbf{E}_p^{n+\theta}, \mathbf{B}_p^{n+\theta}$ acting on the particle p are evaluated at $\mathbf{x}_p^{n+\frac{1}{2}}$, interpolated from the 4 grid points surrounding the particle via a volume $(r^2 - z)$ weighting function W. The plasma current required by Maxwell's equations is loaded to the grid by the same weighting function and is given by:

$$\mathbf{J}_{pl}^{n+\frac{1}{2}} = \sum_s^{N_s} \sum_p^{N_{p(s)}} q_s \mathbf{v}_p^{n+\frac{1}{2}} W \tag{13}$$

where we employ Verboncoeur volume corrections [26] to avoid errors in the charge accumulations arising in curvilinear coordinate systems. In equation (13), N_s is the number of charged species in the plasma and $N_{p(s)}$ the number of simulated particles of a given species s. Every charged particle has the same specific weight w_c (ratio of real particles per simulated particle) independently of the species. We employ absorbing boundary conditions for the charged particles on the plasma chamber, removing them from the computation once they reach the wall.

For the electromagnetic fields, absorbing boundary conditions are required at the edge of the simulation domain to truncate the unbounded space with a finite domain. On a Yee cell, only the electric field components $E_\star$ require specific boundary conditions, as the magnetic ones can be computed by relevant finite difference equations [27]. At the axial ends we employ Mur's boundary condition [27], solving:

$$\left(\frac{\partial E_\star}{\partial z} + \frac{1}{c}\frac{\partial E_\star}{\partial t}\right) = 0 \tag{14}$$

whereas at the radial end we employ the boundary conditions by Bayliss and Turkell [28]:

$$\left(\frac{\partial}{\partial r} + \frac{1}{c}\frac{\partial \Phi}{\partial t} + \frac{1}{2r}\right) E_\star = 0 \tag{15}$$

Both boundary conditions are solved by finite-differences implicitly.

2.3. Solution of the non-linear system

At each time step we seek the solution of $6N_g$ field equations (3 components of $\mathbf{B}^{n+1}$ and 3 of $\mathbf{E}^{n+1}$ on each grid point), together with $6N_{p(s)}N_s$ equations of motion (3 spatial components of $\mathbf{x}_p^{n+1}$ and 3 velocity ones of $\mathbf{v}_p^{n+1}$ for each particle) coupled to each other via $\mathbf{J}$. For a typical simulation with $N_g \approx 10^4$ and $N_p \approx 10^6$–10^7 this would result in matrices whose size is impractical to solve. Following [29] we use a technique called kinetic enslavement which allows embedding the solution of the particles' equations of motion within function evaluations of the EM fields, keeping the matrices' size to the $6N_g$ EM field equations only.

We solve the system of equations (8), (9), (11), (12), (13) using the Jacobian-Free Newton Krylov (JFNK) method available in the NITSOL package [30]. The field equations (8), (9) are first rewritten in residual form:

$$\mathbf{F}(\mathbf{y}) = \mathbf{0} \tag{16}$$

with $\mathbf{y}$ a vector containing the unknowns $\mathbf{B}^{n+1}$, $\mathbf{E}^{n+1}$ and $\mathbf{F}(\mathbf{y})$ a non-linear operator. The non-linearity arises since $\mathbf{J}$ depends on $\mathbf{x}, \mathbf{v}$ which are coupled to $\mathbf{E}, \mathbf{B}$ via equations (11), (12). Using a Newton method, we seek successive approximations to the system (16) based on information about the current guess $\tilde{\mathbf{y}}_k$ and its derivative:

$$\frac{\partial \mathbf{F}(\tilde{\mathbf{y}}_k)}{\partial \mathbf{y}} \delta \mathbf{y}_k = -\mathbf{F}(\tilde{\mathbf{y}}_k) \tag{17}$$

where the increment $\delta \mathbf{y}_k$ defines the new guess:

$$\tilde{\mathbf{y}}_{k+1} = \tilde{\mathbf{y}}_k + \delta \mathbf{y}_k \tag{18}$$

for each Newton iteration k. The resulting system of equations (17) is linear and can be efficiently solved by the Generalized Minimal RESidual (GMRES) method. The Jacobian matrix $\partial \mathbf{F}(\tilde{\mathbf{y}}_k)/\partial \mathbf{y}$ required in (17) at each Newton iteration is approximated by finite-differences. We use the standard NITSOL termination criteria in which iterations are stopped based on an absolute tolerance on the function evaluation $\|\mathbf{F}\| \leq$ ftol, or on a step tolerance: $\|\delta \mathbf{y}_k\| \leq$ stptol, as described in [30].

In the kinetic enslavement technique, the particles' equations of motion are embedded within function evaluations of the system (16). More precisely, at each GMRES iteration the latest guess of the EM fields $\tilde{\mathbf{B}}^{n+1}$ and $\tilde{\mathbf{E}}^{n+1}$ are available in the vector $\tilde{\mathbf{y}}$ and can be used to advance the particles via equations (11), (12). With the new values of the particles' position and velocity we have all the information needed to form a new guess for $\tilde{\mathbf{J}}_{pl}$ via equation (13) and to advance to the next iteration. The operator $\mathbf{F}(\mathbf{y})$ besides containing the spatial discretization operators acting on $\mathbf{B}$ and $\mathbf{E}$ includes the particle mover used to update $\mathbf{x}_p$ and $\mathbf{v}_p$ as shown in Algorithm 1 and section 2.4.

2.4. Particle mover

The particle mover contains the routines used to solve equations (11), (12) leading to the update of $\mathbf{x}_p$ and $\mathbf{v}_p$ at each time step. Within the kinetic enslavement technique the particle mover can be chosen independently from the method used on the field solver, allowing greater freedom on the selection of the numerical techniques used.

To solve the particles' equations of motion (11), (12) we seek to determine $\mathbf{x}_p^{n+1}$ and $\mathbf{v}_p^{n+1}$ based on the information of the grid values $\mathbf{E}^{n+\theta}$ and $\mathbf{B}^{n+\theta}$ stored in the vector $\tilde{\mathbf{y}}$ at each GMRES iteration. While the EM field on the grid is available, the force acting on the particle p depends on the position at half time step $\mathbf{x}_p^{n+1/2}$ which is yet unknown. Starting from the free streaming approximation we first estimate the position $\mathbf{x}_p^{n+1/2} = \mathbf{x}_p^n + \mathbf{v}_p^n \Delta t/2$ that we then subsequently refine by Picard iteration until convergence is reached.

Algorithm 1: Function evaluation routine.

Input: latest guess $\tilde{\mathbf{y}}$, containing $\tilde{\mathbf{B}}^{n+1}$ and $\tilde{\mathbf{E}}^{n+1}$
Calculate $\tilde{\mathbf{B}}^{n+\theta}$ and $\tilde{\mathbf{E}}^{n+\theta}$

```
# For each particle find x̃_p^{n+1/2} and ṽ_p^{n+1/2}:
for s = 1 to N_s do
    for p = 1 to N_p do
        Solve equations of motion (11), (12), see section 2.4
        if x̃_p^{n+1/2} is outside the plasma chamber then
            Do not accumulate contribution to the plasma current
        end
    end
end
```

Calculate $\tilde{\mathbf{J}}_{pl}^{n+\frac{1}{2}}$ via equation (13)
Evaluate residual via equation (16)

The velocity at half time step $\mathbf{v}_p^{n+\frac{1}{2}}$ can be directly computed with an algebraic manipulation of equation (12) as shown in [31]. This leads to:

$$\mathbf{v}_p^* = \mathbf{v}_p^n + \alpha \mathbf{E}_p^{n+\theta} \qquad \text{with: } \alpha = \frac{q_s \Delta t}{2 m_s} \tag{19}$$

$$\mathbf{v}_p^{n+\frac{1}{2}} = \frac{\mathbf{v}_p^* + \alpha \left[\mathbf{v}_p^* \times \mathbf{B}_p^{n+\theta} + \alpha (\mathbf{v}_p^* \cdot \mathbf{B}_p^{n+\theta}) \mathbf{B}_p^{n+\theta} \right]}{1 + (\alpha \mathbf{B}_p^{n+\theta})^2} \tag{20}$$

With $\mathbf{v}_p^{n+\frac{1}{2}}$ available, the position $\mathbf{x}_p^{n+1}$ and velocity $\mathbf{v}_p^{n+1}$ at the new time step are computed as:

$$\mathbf{x}_p^{n+1} = \mathbf{x}_p^n + \Delta t \mathbf{v}_p^{n+\frac{1}{2}} \tag{21}$$

$$\mathbf{v}_p^{n+1} = 2\mathbf{v}_p^{n+\frac{1}{2}} - \mathbf{v}_p^n \tag{22}$$

In cylindrical coordinates one should include the extra inertial forces arising from the curvilinear transformation. Following Boris [32] this can be avoided by employing a local Cartesian coordinate system for each particle. More precisely at each time step n we align a Cartesian frame to the particle position such that $x^n = r^n$, $y^n = 0$ and $z^n = z^n$, with the velocity components $v_x^n = v_r^n$, $v_y^n = v_\theta^n$ and $v_z^n = v_z^n$. The particle advance is then performed in the local Cartesian frame where equations (20), (21), (22) are valid; the updated values are then re-transformed to their respective cylindrical coordinates. During the step, the EM forces acting on the particle must also be rotated to align with the local coordinate frame. The sequence of operations is described in detail in [33], of which we follow the same steps.

Absorbing boundary conditions are imposed at the end of the particle mover: all charged particles with $\mathbf{x}_p^{n+1}$ lying outside the plasma chamber are removed from the computation. Within the kinetic enslavement technique absorbing boundary conditions are only temporarily imposed as each iteration only represent an approximation of the new particle position. In this case if a particle exits the plasma chamber at $\tilde{\mathbf{x}}_p^{n+\frac{1}{2}}$ its contribution to the plasma current is neglected, while maintaining the particle alive for the next JFNK iteration.

2.5. Monte Carlo Collision method

Particle collision processes (term F_c in equation (7)) are taken into account via a Monte Carlo Collision (MCC) method, in which electron-neutral, electron-ion and ion-neutral collisions are handled via a null-collision method [34], whereas Coulomb collisions are treated with the binary collision method [35] following the work of [36]. The sampling of the null-collision is performed on each cell to take into account the local density of the target particles.

We implemented the model for a hydrogen discharge; the list of cross-sections and the respective references are listed in Table 1, 2. Following [34] we employ a constant time-step approach, in which collisions are calculated separately from the motion of the particles and only need to be evaluated between time steps, see Algorithm 2. The method requires the collision time-step Δt_{coll} to be much smaller than the mean free time τ. Empirically we observe no difference in the results as long as $\Delta t_{coll} < \tau/100$. The mean free time τ is calculated for each species as the inverse of the maximum collision frequency ν_{max} in the energy range considered of 0–200 eV. When a collision happens, a partner particle is selected in the same cell. The post-collision energies are taken from [37] with their respective velocities isotropically distributed [34]. In all simulations we employ $\Delta t = \Delta t_{coll}$.

Table 1
Electron impact processes.

Partner	Reaction	Formula	Reference
H	Elastic	$e + H \longrightarrow e + H$	[38]
	Electr. exc.	$e + H \longrightarrow e + H(nl)$	[39]
	Ionization	$e + H \longrightarrow e + H^+ + e$	[39]
H_2	Elastic	$e + H_2 \longrightarrow e + H_2$	[40]
	Vibr. exc.	$e + H_2(v = 0) \longrightarrow e + H_2(v = 1, 2)$	[39] ⋆
		$e + H_2(v \geq 1) \longrightarrow e + H_2(v \pm 1)$	[41] ⋆
		$H_2(B^1\Sigma_u^+) \longrightarrow H_2(v') + h\nu$	[42]
		$H_2(C^1\Pi_u) \longrightarrow H_2(v') + h\nu$	[42]
	Electr. exc.	$e + H_2(v) \longrightarrow e + H_2(B^1\Sigma_u^+)$	[39]
		$e + H_2(v) \longrightarrow e + H_2(C^1\Pi_u)$	[39]
		$e + H_2(v = 0) \longrightarrow$ $\longrightarrow e + H_2(B', B'', D, D', EF)$	[39]
	Diss. via b^3	$e + H_2(v) \longrightarrow e + H_2(b^3\Sigma_u^+) \longrightarrow$ $\longrightarrow e + H + H$	[39]
	Nondiss. ioniz.	$e + H_2(v) \longrightarrow e + H_2^+ + e$	[39]
	Diss. ioniz.	$e + H_2(v) \longrightarrow e + H_2^+(^2\Sigma_u^+) + e \longrightarrow$ $\longrightarrow e + H^+ + H + e$	[39]
	Diss. attach.	$e + H_2(v) \longrightarrow H + H^-$	[39]
H_2^+	Diss. exc.	$e + H_2^+ \longrightarrow e + H^+ + H$	[39]
	Diss. recomb.	$e + H_2^+ \longrightarrow H + H$	[39]
	Diss. ioniz.	$e + H_2^+ \longrightarrow e + H^+ + H^+ + e$	[39]
H_3^+	Diss. exc.	$e + H_3^+ \longrightarrow e + H^+ + 2H$	[39]
	Diss. recomb.	$e + H_3^+ \longrightarrow 3H$	[39]
H^-	e-detach.	$e + H^- + \longrightarrow e + H + e$	[39]

⋆ inverse processes evaluated by detailed balance

Table 2
Ion impact processes.

H^+ impact processes

Partner	Reaction	Formula	Reference
H	Elastic	$H^+ + H \longrightarrow H^+ + H$	[43]
	Charge Exc.	$H^+ + H \longrightarrow H + H^+$	[39]
H_2	Elastic	$H^+ + H_2 \longrightarrow H^+ + H_2$	[43]
	Vibr. exc.	$H^+ + H_2(v = 0) \longrightarrow H^+ + H_2(v = 1\text{–}4)$	[39] ⋆
	Dissociation	$H^+ + H_2(v) \longrightarrow H^+ + H + H$	[39]

H_2^+ impact processes

Partner	Reaction	Formula	Reference
H_2	Charge exc.	$H_2^+ + H_2 \longrightarrow H_2 + H_2^+$	[39]
	CID	$H_2^+ + H_2 \longrightarrow H^+ + H + H_2$	[39]
	H_3^+ ion form.	$H_2^+ + H_2 \longrightarrow H_3^+ + H$	[39]

H_3^+ impact processes

Partner	Reaction	Formula	Reference
H_2	Elastic	$H_3^+ + H_2 \longrightarrow H_3^+ + H_2$	[44]
	Proton transfer	$H_3^+ + H_2 \longrightarrow H_2 + H_3^+$	[39]
	CID to proton	$H_3^+ + H_2 \longrightarrow H^+ + H_2 + H_2$	[39]
	CID to H_2^+	$H_3^+ + H_2 \longrightarrow H_2^+ + H + H_2$	[39]

H^- impact processes

Partner	Reaction	Formula	Reference
H^+	Mutual neutr.	$H^- + H^+ \longrightarrow H + H$	[39]
H	Res. ch. exc.	$H^- + H \longrightarrow H + H^-$	[39]
	Assoc. detach.	$H^- + H \longrightarrow e + H_2$	[39]
	NA detach.	$H^- + H \longrightarrow e + H + H$	[39]
H_2	e-detach.	$H^- + H_2(v) \longrightarrow H + H_2(v') + e$	[39]

2.6. Neutrals treatment

In a typical ICP discharge the ionization degree reaches values of a few %, implying that the largest populations are represented by neutrals. Their spatial distribution can be non-uniform in the plasma chamber, with depletion arising in the regions of highest ionization rate [45]. In molecular discharges (e.g. hydrogen) one must also take into account the long lived vibrational states, since those have significant effect on the electron and ion impact cross-sections [39].

We have implemented a neutral transport module for hydrogen, solving kinetically the equations of motion of the atomic H^0 and the 15 vibrational states of the molecular $H_2(v)$. The electronic excited states of H^0 and H_2 are not tracked in the present case given their short decay time. Electronic excitation processes are nevertheless considered in the reaction set and represent an energy sink for electrons and ions. To cope with the high density and large number of species, we employ a variable weight scheme using a rezoning technique [46]. More precisely, each neutral particle has associated its own specific weight w_n (ratio of real particles per simulated one). The scheme aims at keeping a constant number of neutral particles per species per cell $\bar{N}_n$ (typically 100), merging and splitting the simulated particles following the density variations due to transport or collisions. When the number of particles in a cell $N_n > \bar{N}_n$, following algorithm C1 in [46], we select the two closest particles of the concerned species $p = 1, 2$ in phase space and replace them with a single one $p = A$ with the weighted average position, velocity and the sum of their weights w: $w_A = w_1 + w_2$, $\mathbf{x}_A = (w_1\mathbf{x}_1 + w_2\mathbf{x}_2)/w_A$, $\mathbf{v}_A = (w_1\mathbf{v}_1 + w_2\mathbf{v}_2)/w_A$. Similarly, if at any time the number of particles per cell $N_n < \bar{N}_n$ following algorithm S1 in [46] we split the particle with the highest weight $p = A$ in four particles $p = 1, 2, 3, 4$ with the properties: $w_p = w_A/4$; $r_{1,2} = r_A \pm \Delta r/\bar{N}_n$, $r_{3,4} = r_A$; $\theta_{1,\dots,4} = \theta_A$; $z_{3,4} = z_A \pm \Delta z/\bar{N}_n$, $z_{1,2} = z_A$. With this technique the maximum number of neutral particles to be simulated is $16N_g\bar{N}_n$ (with 16 is the number of neutral species).

For compatibility with the MCC scheme, the range of neutral weights is larger and a multiple of the charged particle weights, i.e. $w_n \geq w_c$. This because in the event of a collision, only a fraction of the neutral particle corresponding to w_c must be considered in evaluating the post-collisional velocities, while leaving the fraction $w_n - w_c$ unaffected on its trajectory. If $w_n < w_c$ the scheme would be inconsistent. In practice therefore the merging technique is applied only when there are at least $N_n = \bar{N}_n$ particles in a cell all with at least $w_n = w_c$. Splitting is also avoided for particles with $w_n \leq 4w_c$.

The equation of motion for the neutrals only includes a collisional force as no EM field acts on them (equation (7)). This accounts for collisions with other particles or wall interactions. Since no change in velocity happens during a time step (section 2.5), the equation of motion for the neutrals can therefore be solved directly with:

$$\mathbf{x}_p^{n+1} = \mathbf{x}_p^n + \Delta t\mathbf{v}_p^n \tag{23}$$

At the wall we employ a simple reflection boundary condition for H_2, inverting the velocity components in the directions in which the particle interacts with the wall. For H^0 wall recombination into H_2 is taken into account by a user-defined recombination coefficient γ_w that defines the reflected species by random sampling.

3. Code implementation

In this section we describe details of the NINJA code implementation (written in Fortran90) and additions to the model presented in order to improve its performance. Firstly, we find it convenient to express the operator $\mathbf{F}(\mathbf{y})$ in matrix form:

$$\mathbf{F}(\mathbf{y}) = \mathbf{A}\mathbf{y} - \mathbf{b} - \mathbf{J}_{pl}(\mathbf{y}) = \mathbf{0} \tag{24}$$

where the matrix $\mathbf{A}$ contains the discrete spatial operator acting on $\mathbf{B}^{n+1}$, $\mathbf{E}^{n+1}$; $\mathbf{b}$ is the known term from the time step n and $\mathbf{J}_{pl}(\mathbf{y})$ is the plasma current which is a function of $\mathbf{y}$. This formulation is advantageous as, upon formation of the plasma current at each GMRES iteration, it leads directly to a vectorized implementation. Furthermore the matrix $\mathbf{A}$ has by construction a very low density and can efficiently be stored in sparse format, while $\mathbf{b}$ is a constant term at each time step and can be precomputed outside JFNK. For all sparse matrix computations we employ the SPARSKIT library [47]. The time loop proceeds therefore as illustrated in Algorithm 2.

Secondly, while SI units are convenient to describe the governing equations, they are not well suited for numerical computation as the numbers to be treated vary by many orders of magnitude. This may lead to a badly conditioned problem as well as to floating point rounding errors. To avoid these issues, we apply a normalization for which $\epsilon_0 = \mu_0 = 1$ leading to a speed of light $c = 1$. Furthermore we normalize time to the time step, mass to the electron mass and temperature to 1 eV. All other units follow accordingly. The conversion to normalized units is performed internally in the code, leaving inputs and outputs in SI units for ease of interpretation. As an example of the benefit of this transformation, the condition number of the matrix $\mathbf{A}$ decreases from $k(\mathbf{A}) > 10^{14}$ in SI units to $k(\mathbf{A}) = \mathcal{O}(10)$ in normalized units for typical simulation parameters.

In terms of performance, code profiling for a typical simulation with $N_g = 10^4$ and $N_p = 10^6$–10^7 reveals that the majority of the computing time (> 90%) is spent in the particle mover. Within the kinetic enslavement technique, at each function evaluation (Algorithm 1) the full set of particles needs to be moved to calculate the new guess of the plasma current. This indicates that improvements in the code performance can be achieved either by seeking techniques to reduce the number of iterations required to achieve convergence in JFNK at each time step, or by parallelizing the computation, i.e. distributing the particles over several processes.

Algorithm 2: Time loop.

```
for t = 1 to N_iter do
    Calculate b in equation (24)

    # Find B^{n+1} and E^{n+1} with JFNK:
    while ||F|| ≤ ftol, or ||δy_k|| ≤ stptol do
        Function evaluation via Algorithm 1
    end
    # Charged particles push
    For each particle p calculate x_p^{n+1} and v_p^{n+1}
    if x_p^{n+1} is outside the plasma chamber then
        delete particle
    end
    # Neutrals treatment
    Neutral particles push, for each neutral h calculate x_h^{n+1} and v_h^{n+1}
    if x_h^{n+1} is outside the plasma chamber then
        reflection or recombination
    end
    Perform neutrals merging/splitting

    # Evaluate collisions
    Monte Carlo Collision module
end
```

3.1. Preconditioning

To improve the performance of the code, it is highly desirable to reduce the number of GMRES iterations for each Newton step, which can be achieved by preconditioning the linear system (equation (17)). An efficient preconditioner should represent an approximation of the Jacobian matrix $\partial \mathbf{F}(\tilde{\mathbf{y}}_k)/\partial \mathbf{y}$. From equation (24) we observe that the Jacobian matrix contains two components: the matrix $\mathbf{A}$ and a term depending on the plasma current. While the first term is known and constant, the second depends on the particular solution at any given GMRES iteration and it is not straightforward to calculate.

We employ a simple preconditioner in which the contribution acting on the plasma current is neglected. This represents a crude approximation of the Jacobian, which is sufficient to cut the number of GMRES iterations as long as the time step is not too large (see section 5.4). More precisely, we perform an incomplete Lower–Upper (LU) factorization of the matrix $\mathbf{A}$ with the *ilut* routine from SPARSKIT, which is later supplied to the *lusol* routine of the same library for the preconditioning within the NITSOL solver.

3.1.1. Parallelization

Code parallelization is implemented with the MPI interface, in which we use a domain decomposition technique at the particle level, while the EM calculation is performed serially on the full simulation domain. During the simulation time, density variations may cause the load on each process to be unbalanced. Therefore the total number of particles on each process is constantly monitored and compared to the average value, calculated as the total number of particles divided by the number of processes. If the load unbalance is $> 10\%$, the subdomains are resized to host an approximately equal number of particles, while maintaining the boundary between sub-domains to coincide with cell's boundaries, to facilitate the treatment of the neutrals that require a constant number of particles per cell.

4. Electromagnetic fields in the plasma, comparison with analytic results

As a first code application we wish to present the simulation of an RF-ICP in the "infinitely-long configuration", for which analytic solutions of the radial electromagnetic field profiles exist and provide a verification step for the code developed. Following [23], in the case of a uniform plasma density, the complex amplitudes of $H_z(r)$ with $H_z = B_z/\mu_0$ and $E_\theta(r)$ are given by:

$$H_z(r) = H_{z0}\frac{J_0(kr)}{J_0(kr_0)} \tag{25}$$

$$E_\theta(r) = \frac{-ikH_{z0}}{\omega\epsilon_0\epsilon_p}\frac{J_1(kr)}{J_0(kr_0)} \tag{26}$$

where $H_{z0} = H_z(R)$, $k = k_0\sqrt{\epsilon_p}$ is the complex wavenumber in the plasma, ϵ_p is the plasma complex permittivity, $k_0 = \omega/c$ is the wavenumber in free space and J_n represent the Bessel function with complex argument of order n.

We performed a set of simulations on a domain with $R = 20$ mm, $L = 200$ mm (see Fig. 1), with a coil spanning the whole plasma chamber length with internal and external radii of 24 and 26 mm respectively. The plasma is initially uniformly loaded in the plasma chamber with densities ranging from 10^{16} to 10^{18} m^{-3} and the RF current is adjusted to

Table 3
Simulation parameters and initial conditions for the RF-ICP in "infinitely long" configuration.

Parameters		Initial conditions	
Cell size	1×1 mm	N. particles	5'000'000
Time step	$2.5 \cdot 10^{-11}$ s	e^- density	10^{16}, 10^{17}, 10^{18} m^{-3}
Implicit param. θ	0.6	e^- temp.	1 eV
Particle weight	10^6, 10^7, 10^8	$H^+ : H_2^+ : H_3^+$	0.4:0.4:0.2
RF current	120, 160, 350 A	Ion temp.	0.1 eV
RF coil turns	1	Gas temp.	300 K
RF frequency	13.56 MHz	Vib. temp.	3000 K
Gas pressure p_{H_2}	1 Pa (@300K)	Diss. Degree	0.3
Wall recomb. γ_w	10^{-3}		
ftol, stptol	10^{-4}, 10^{-5}		

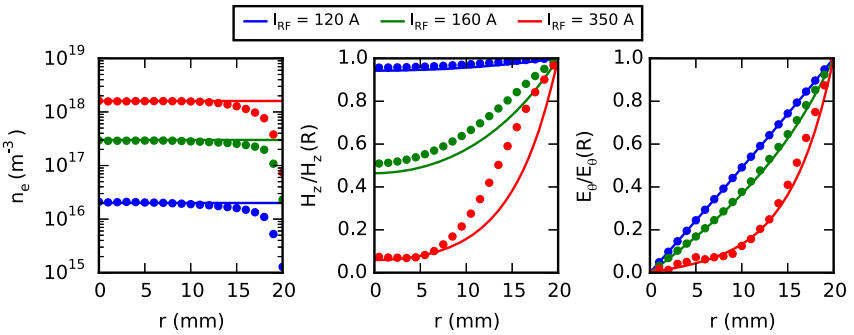

Fig. 2. Comparison between analytical estimates (solid line) and simulation results (dots) of the electron density and electromagnetic fields radial profiles in the plasma chamber for the RF-ICP in "infinitely-long configuration". (For interpretation of the references to color in this figure legend, the reader is referred to the web version of this article.)

maintain the plasma discharge approximately at the same average density. The integration time is 5 μs corresponding to 67 RF cycles at 13.56 MHz, time at which no change in the EM profile nor in the density profile is observed. The simulation parameters are reported in Table 3.

Fig. 2 shows the comparison between the analytic estimates and the simulation results, evaluated at $z = 100$ mm (axial center of the plasma chamber) to best approximate the "infinitely long" configuration. The average value of the simulated density profile is used as input for the analytic calculation. An excellent agreement is found in the prediction of E_θ, whereas a slight underestimation of H_z results in the simulations particularly in the region close to the wall. This however could result from the difference in the density profiles, which is assumed uniform in the analytical estimate in contrast to the simulations where it is self-consistently calculated, leading to a drop close to the wall.

The density range analyzed corresponds to a variation of $\Delta x/\lambda_{De}$ from 1 to 20. The agreement with the analytic solutions is a first indication of the code capability to simulate the plasma dynamics in RF-ICP with cell sizes in excess of the Debye length.

5. Simulation of the Linac4 H^- ion source plasma generator

We present an application of the NINJA code for the plasma simulation of the Linac4 H^- ion source at CERN [3], whose geometry is shown in Fig. 3. The plasma chamber has a radius of 24 mm and a length of 136 mm, surrounded by a 5 turn RF coil operated at 2 MHz. At one end of the plasma chamber a 45° molybdenum electrode is installed, which is taken into account in the model by a staircase grid. No external magnetic fields are taken into account in the present study. The simulation domain is taken 3 times larger than the plasma chamber to avoid large reflections at the end of the domain. The simulation parameters and the initial conditions are listed in Table 4. The plasma is initially seeded uniformly in the plasma chamber in a neutral state, i.e. the ion density equals to the electron plus the negative ion density. Neutrals are also initially seeded uniformly in the plasma chamber with a user-defined dissociation degree.

The choice of the cell size and time step follows from an analysis of the spatio-temporal scales of interest in the plasma under investigation. More precisely, it is known that in an ICP the power transfer from the coil RF field to the electrons happens in a skin depth δ close to plasma chamber wall where the coil is located [48]. This represents a critical scale length for the simulation of ICPs and the cell size should therefore be sufficiently fine to resolve its dynamics. For the pressure and driving frequency employed an estimate of δ can be obtained as shown in [48]:

$$\delta = \frac{c\sqrt{2}}{\omega_{pe}}\sqrt{\frac{\nu}{\omega}} \tag{27}$$

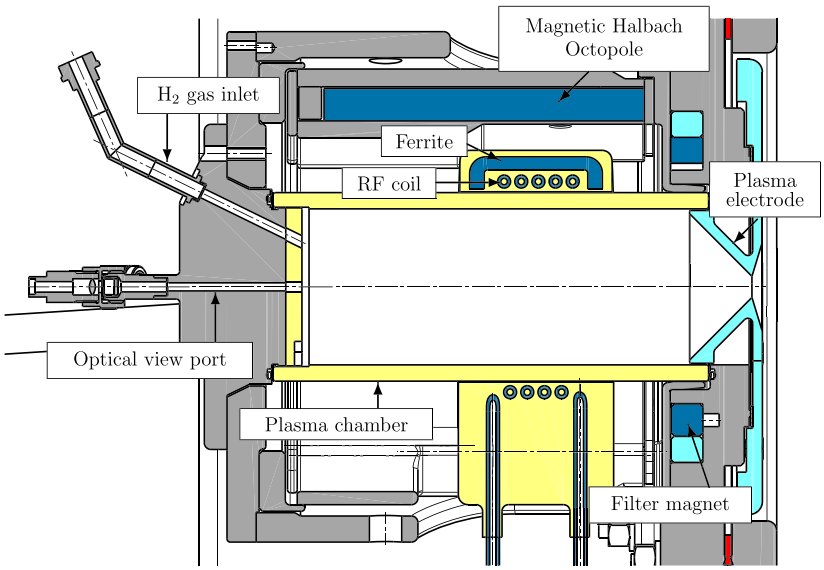

Fig. 3. Plasma generator of the Linac4 H^- ion source. The plasma chamber has a radius of 24 mm and a length of 136 mm. The 5 turn RF coil is surrounded by 6 ferrites and embedded in epoxy to avoid RF breakdown. The H_2 gas inlet and the optical view port used to perform optical emission spectroscopy measurements are indicated. The magnetic Halbach octupole is formed by alternating magnets with clockwise and counter-clockwise magnetization, while the filter field is a dipole magnet with vertical magnetization. The plasma electrode has an angle of 45° and is made of molybdenum.

Table 4
Simulation parameters and initial conditions.

Parameters		Initial conditions	
Cell size	1×1 mm	Particle number	448'624
Time step	$2.5 \cdot 10^{-11}$ s	e^- density	$5 \cdot 10^{17}$ m^{-3}
Implicit parameter θ	0.6	e^- temp.	1 eV
Particle weight	$5 \cdot 10^8$	$H^+ : H_2^+ : H_3^+$	0.8:0.1:0.1
RF coil current	70 A	Ion temp.	0.1 eV
RF coil turns	5	Gas temp.	300 K
Gas pressure p_{H_2}	3 Pa (@300K)	Vib. temp.	3000 K
Wall recomb. γ_w	10^{-3}	Diss. Degree	0.3
ftol, stptol	10^{-4}, 10^{-5}		

where c is the speed of light, ω_{pe} the plasma frequency, ν the collision frequency and ω the angular frequency of the applied RF. For the case considered with $n_e \approx 10^{19}$ m^{-3} (taken from previous simulations and experimental results [49]), $\nu \approx 3.6 \cdot 10^7 p_{H_2} \approx 10^8$ Hz [50] we obtain $\delta \approx 7$ mm. The cell size is chosen in the range $0.5 \leq \Delta x \leq 4$ mm.

For the time scales, the strictest condition is represented by the collision frequency ν implying that $\Delta t < 10^{-10}$ s to satisfy the Monte Carlo condition $\Delta t < \tau/100$ with $\tau = 1/\nu$. Such time step allows a fine resolution of the driving frequency and several of its harmonics.

We first present a simulation with $\Delta r \times \Delta z = 1 \times 1$ mm, $\Delta t = 2.5 \cdot 10^{-11}$ s and $\theta = 0.6$. The plasma distribution and the impact of the cell size on the simulation results is discussed in section 5.1, the Electron Energy Distribution Function (EEDF) is shown in section 5.2 and the energy conservation in section 5.3.

5.1. Plasma distribution

Starting from the initial uniform distribution we follow the plasma dynamics to reach steady state after 15 µs. Fig. 4 shows the electron density and energy profile averaged in time during the last RF cycle (0.5 µs) of simulation. The electron density peaks at $n_e = 10^{19}$ m^{-3} on the central axis of the plasma chamber, in the axial region where the coil is located. The highest electron energy E_e is located in the coil region, with the hottest electrons in the vicinity of the radial wall where the RF electric field is strongest. At steady state the ion population is comprised of 85% H^+, 10% H_2^+ and 5% H_3^+, while H^- represent 1% of the negative charges. The total number of simulated charged particles at steady state is ≈ 3 million. For completeness, the normalized quantities are: $\omega_{pe}\Delta t \approx 4.25$, $\Delta x/\lambda_{De} \approx 60$, $v_{th}\Delta t/\Delta x \approx 0.025$. The simulation time is 2 weeks on a 12 core cluster (64 GB RAM with Intel(R) Xeon(R) CPU E5-2630L @ 2.00 GHz, no hyper-threading). The normalized variation of the simulation results as a function of the cell size is better visualized on a line profile. Fig. 5 shows the radial profile of n_e and E_e in the center of the coil, i.e. $z = 70$ mm. For a cell size ≤ 1 mm no significant difference is observed neither in the density nor the energy distribution. For larger cell sizes, the grid does not have the required

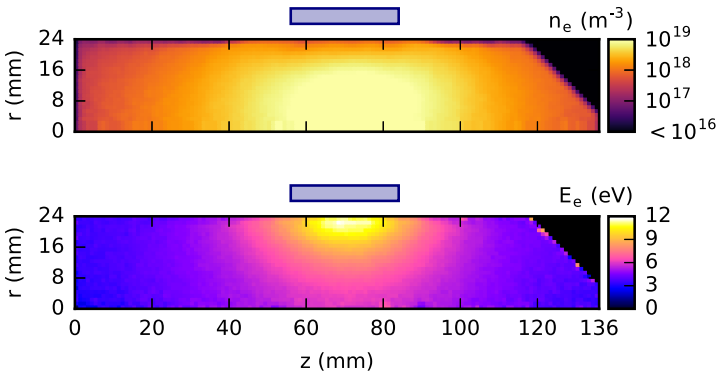

Fig. 4. Electron density (top) and electron energy (bottom) profiles, time-averaged during the last RF cycle of simulation. The location of the RF coil is indicated by the blue rectangle. (For interpretation of the references to color in this figure, the reader is referred to the web version of this article.)

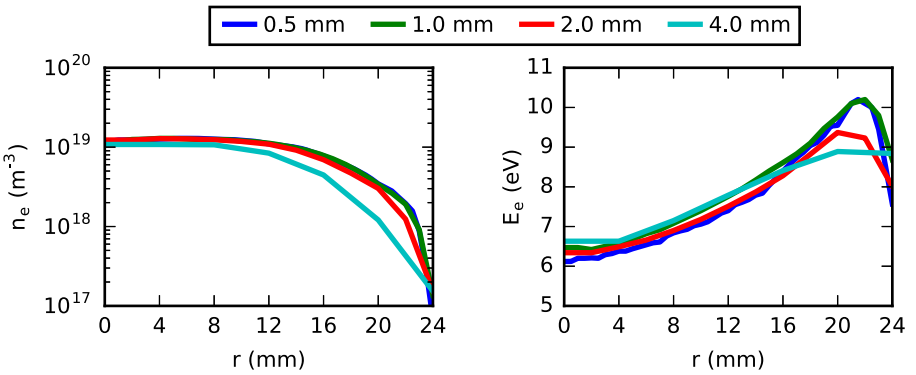

Fig. 5. Electron density n_e and energy E_e radial profile in the center of the coil, i.e. $z = 70$ mm for different cell sizes (0.5, 1.0, 2.0 and 4.0 mm). All simulations are performed with $\Delta t = 2.5 \cdot 10^{-11}$ s and $\theta = 0.6$ and the profile represents the time averaged value in the last RF cycle of simulation. (For interpretation of the references to color in this figure legend, the reader is referred to the web version of this article.)

resolution to capture the large gradients present in the skin depth and a different trend is observed, particularly in the region close to the wall $16 \leq r \leq 24$ mm.

5.2. Electron Energy Distribution Function

One of the most important characteristics of kinetic models is the self-consistent calculation of the EEDF in the plasma. From NINJA we can obtain the EEDF for any plasma region as a function of time. As an example we present the EEDF as a function of time during the last RF cycle in the region $0 \leq r \leq 4$ mm and $0 \leq z \leq 136$ mm. The region is selected to allow a direct comparison with Optical Emission Spectroscopy (OES) measurements performed on the axial view port of the plasma chamber (Fig. 3) [49].

Fig. 6 shows the EEDF at two specific times corresponding to the RF current phase $\phi = 0$ and $\phi = \pi/2$. A deviation of the high energy tail ($E_e > 15$ eV) of the EEDF is observed as a function of time. The time averaged-value, calculated from 16 EEDF snapshots during the last RF cycle, is well approximated by a Maxwellian distribution with $T_e = 4$ eV.

Previous studies [51] performed in low density regime showed that the EEDF deviation from Maxwellian is related to the acceleration of electrons from the inductive electric field. The impact is particularly noticeable for the high energy tail of the EEDF as the cross-section of Coulomb collisions decreases for increasing energies, whereas the frequent collisions at low energy lead to thermalization. It must be noted however that artificial thermalization effects could arise in PIC-MCC simulations [52] and further studies and experimental data will be required to assess their impact on the simulation results.

5.3. Energy and charge conservation

Monitoring of the conservation laws represents a crucial diagnostics to verify the implementation and the choice of the numerical parameters. If the total energy increases over time, it is an indication that numerical heating is taking place, which might lead to unphysical results. If the energy decreases, the method remains stable but one must be careful that important physics of interest is not suppressed. If charge is not conserved, the divergence equation (1) is no longer satisfied, which may impact the simulation results.

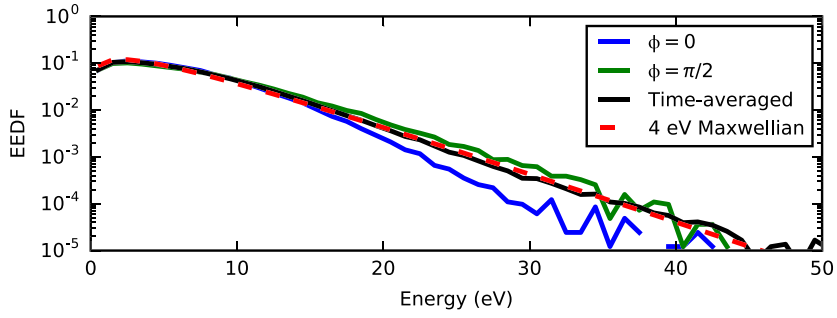

Fig. 6. Electron Energy Distribution Function (EEDF) for the RF current as a function of time during the last RF cycle of simulation in the region $0 \leq r \leq 4$ mm and $0 \leq z \leq 136$ mm. The time-averaged value fits a Maxwellian distribution of $T_e = 4$ eV. (For interpretation of the references to color in this figure legend, the reader is referred to the web version of this article.)

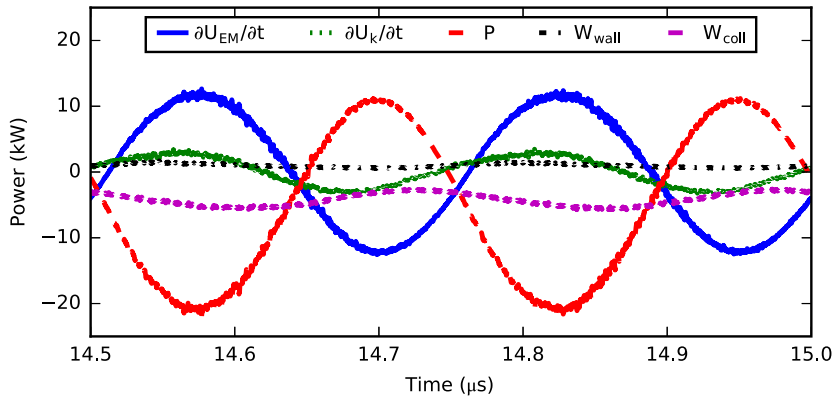

Fig. 7. Time variation of the energy components (see equation (28)) for the simulation with $\Delta r \times \Delta z = 1 \times 1$ mm, $\Delta t = 2.5 \cdot 10^{-11}$ s and $\theta = 0.6$ during last RF cycle of simulation, representing the condition at steady state. All components show a 4 MHz oscillation corresponding to double the driving frequency of 2 MHz.

The conservation of electromagnetic energy is given by the Poynting theorem:

$$\frac{\partial}{\partial t}(U_{EM} + U_k) = -P + W_{coll} - W_{wall} \tag{28}$$

$$\text{with: } U_{EM} = \int_V (\epsilon_0 \mathbf{E}^2 + \mathbf{B}^2/\mu_0) \tag{29}$$

$$U_k = \sum_s \sum_p^{N_{p,s}} m_s v_p^2/2 \tag{30}$$

$$P = \oint_{\partial V} (\mathbf{S} \cdot \hat{n}) dA \tag{31}$$

where U_{EM} represents the energy stored in the fields $\mathbf{B}$ and $\mathbf{E}$, the kinetic energy U_k is given by the sum of the kinetic energy of all particles and P represents the flux through the surface, which is given by the integral of the Poynting vector $\mathbf{S} = \mathbf{E} \times \mathbf{B}/\epsilon_0$. The collisional power W_{coll} represent the energy, per unit of time, lost or gained by the charged particles in elastic or inelastic collisions (e.g. threshold energy lost by an electron in an atomic excitation process). The component W_{wall} represents the power deposited on the wall, i.e. the kinetic energy of the charged particles lost on the wall per unit of time.

Fig. 7 shows the time-varying components of equation (28) for the simulation with $\Delta r \times \Delta z = 1 \times 1$ mm, $\Delta t = 2.5 \cdot 10^{-11}$ s and $\theta = 0.6$ during last RF cycle of simulation, representing the condition at steady state. The variation of all components show a 4 MHz oscillation, double the RF driving frequency. To evaluate the energy conservation we calculate the difference between the left-hand side and the right-hand side of equation (28), integrated in space over the plasma chamber volume, in time during the last RF cycle and normalized it to the RMS value of the left-hand side. The result for different simulation conditions is shown in Fig. 8, where one parameter is varied while keeping the others fixed based on the reference simulation of $\Delta r \times \Delta z = 1 \times 1$ mm, $\Delta t = 2.5 \cdot 10^{-11}$ s and $\theta = 0.6$.

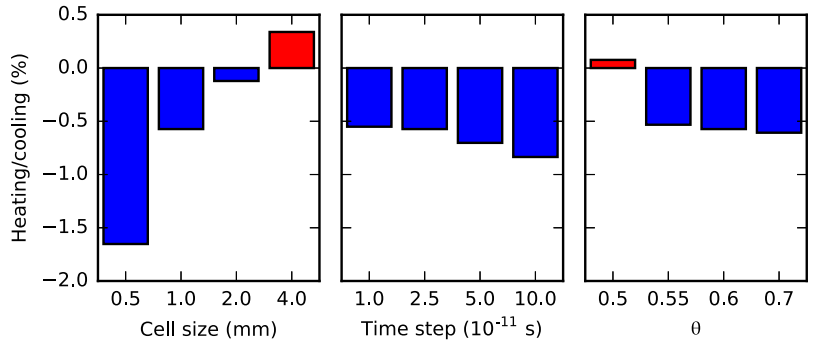

Fig. 8. Impact of the cell size, time step and implicit parameter θ on the energy conservation. Simulations are performed by varying only one parameter at the time, while keeping the others fixed based on the reference simulation of $\Delta r \times \Delta z = 1 \times 1$ mm, $\Delta t = 2.5 \cdot 10^{-11}$ s and $\theta = 0.6$. Energy conservation is evaluated during last RF cycle of simulation, representing the condition at steady state. Blue represents numerical cooling, while red numerical heating. In all simulations energy is conserved within 2%. (For interpretation of the references to color in this figure, the reader is referred to the web version of this article.)

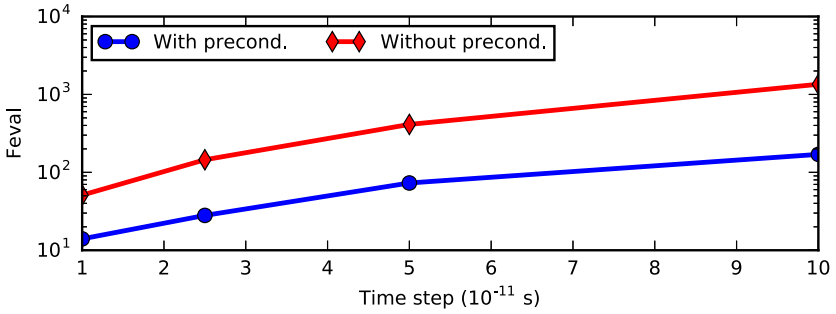

Fig. 9. Average number of function evaluations (Feval) required to reach convergence at each time step within JFNK. All simulations are performed with $\Delta r \times \Delta z = 1 \times 1$ mm and $\theta = 0.6$.

The variation of the cell size indicates that, for a fixed Δt and θ, we have a tendency towards numerical heating by increasing the cell size. Increasing Δt or θ leads on the other hand to larger cooling rates, indicating that stronger damping is taking place. In other words, the choice of the numerical parameters is of paramount importance to control the energy conservation in the simulations, with smaller cell sizes requiring less numerical damping to conserve the energy. We remark that in the parameter range investigated, all simulations show an energy conservation within 2%. In the cases analyzed numerical heating did not lead to unphysical results nor blow-up. However these could arise for longer integration times and the use of the code in these conditions is not recommended.

Charge conservation has been monitored in all simulations to ensure that Gauss' law (equation (1)) is satisfied. This is required because the interpolation of the current density to the grid is not exactly charge conserving and may lead to unphysical results [22]. The error in charge conservation $\mathcal{E}_{Gauss}$ is calculated over the entire grid and the maximum value is recorded for over the entire simulation time:

$$\mathcal{E}_{Gauss} = \frac{\max|\nabla \cdot E - \rho/\epsilon_0|}{\max|\rho|} \tag{32}$$

In all simulations presented $\mathcal{E}_{Gauss}$ remained in the order of 10^{-5} indicating that no significant violation of Gauss' law results.

5.4. Performance

Code performance largely depends on the number of iterations required to reach convergence at each time step in JFNK. We performed an investigation of the number of function evaluations (Feval) required as a function of the time step and evaluate the effectiveness of the preconditioner. Fig. 9 shows the number of Feval for a simulation with $\Delta r \times \Delta z = 1 \times 1$ mm and $\theta = 0.6$. The preconditioner cuts by a factor 3 to 8 the number of Feval required to reach convergence, leading to an equivalent improvement in the computational time.

The benefit of the implicit formulation can be appreciated by estimating the computational cost with respect to its explicit counterpart. Following [21] the computational cost is given by:

$$CPU = \frac{T}{\Delta t} N_p \left(\frac{L}{\Delta x}\right)^d C \tag{33}$$

With T the time-span of the simulation, N_p the number of particles per cell, L the simulation domain, d the number of dimensions and C the solver complexity. By assuming that the implicit solver is the number of function evaluations N_{FE} more complex than the explicit counterpart and with $d = 2$ we obtain:

$$\frac{CPU_{exp}}{CPU_{imp}} = \frac{\Delta t_{imp}}{\Delta t_{exp}} \left(\frac{\Delta x_{imp}}{\Delta x_{exp}} \right)^d \frac{1}{N_{FE}} \tag{34}$$

For the Linac4 ion source application with $n_e = 10^{19}$ m^{-3}, $T_e = 4$ eV and taking in the explicit case $\Delta x = \lambda_{De} = 1.5 \cdot 10^{-5}$ m, and $\Delta t = \Delta x/c$ (c the speed of light), whereas in the implicit case the values used of $\Delta x = 1$ mm, $\Delta t = 2.5 \cdot 10^{-11}$ s, $N_{FE} = 30$ we obtain:

$$\frac{CPU_{exp}}{CPU_{imp}} \approx 70000 \tag{35}$$

showing that a significant improvement results from the implementation.

6. Discussion

A key feature of the model presented is the capability of simulating high density, low temperature plasmas with a cell size $\Delta x \gg \lambda_{De}$ while maintaining the an accurate control the energy conservation. This is of paramount importance to guarantee accuracy and stability for long integration time.

The numerical parameters controlling the energy conservation are the cell size Δx, the time step Δt and the implicit parameter θ. Based on our experience the recommended approach is to first choose Δx sufficiently fine to resolve the smallest spatial scale of interest; in the present case this is represented by the plasma skin depth δ required to capture the current channel in the vicinity of the RF coil. Other applications might require the detailed structure of the plasma sheath and therefore a much smaller cell size. Secondly, the time step should be chosen to resolve the temporal scales of interest including the driving frequency, the Monte Carlo condition on the collision frequency $\Delta t < \tau/100$ as well as resolving the electron gyro-frequency in case of magnetized plasmas. On the lower bound Δt is limited by preserving the energy conservation, together with the parameter θ. As Δt also strongly influences the performance, it is preferable to select Δt to be the most computationally efficient and adjust θ to conserve the energy. Should the range $0.5 \leq \theta \leq 1.0$ not be sufficient, Δt should be modified accordingly to preserve the energy conservation. While we have not pursued this option, in principle Δt and θ could be adapted dynamically during the simulation. These results are in agreement with previous analytical investigation of the energy conservation as a function of θ which has been performed in detail in [25] for an implicit moment method. We would like to point out that in the case of unbounded, collision-less plasmas, the integration with $\theta = 0.5$ is exactly energy conserving as shown in the simulations performed in [22]. The conservation of energy for the cases presented is an indication that an effective suppression of the finite-grid instability is achieved with $\Delta x \gg \lambda_{De}$, hence suppressing the unresolved scales, e.g. plasma oscillations. These empirical results should nevertheless be extended by a detailed finite-grid analysis [53] which will be the object of future studies.

Concerning the code performance, the computational time scales linearly with the number of function evaluations N_{FE} required at each time step. The simple preconditioner employed is capable of cutting N_{FE} by a factor 3 to 8 depending on the time step. Further improvements could be achieved by employing a more sophisticated preconditioner, taking into account the plasma current component, e.g. [54]. Moreover, the domain decomposition technique only at the particle level only allows to parallelize $\approx 95\%$ of the computational cost in a typical scenario (case analyzed of the Linac4 ion source). According to Amdahl's law with 95% parallelizable code a maximum speedup of 20 can be achieved. A better scalability can be obtained by parallelizing the EM field calculation and the I/O procedures.

The range of plasma density and temperature simulated agrees with OES measurements performed on the plasma generator of the Linac4 H^- ion source [49] in similar conditions. Along the central optical view port, OES measurements report a line-integrated plasma density in the range $n_e = 10^{19}$ m^{-3} with an electron temperature $3.5 \leq T_e \leq 4$ eV. The results presented give an average value over the central 4 mm radius of $n_e = 5 \cdot 10^{18}$ m^{-3} with a time-averaged Maxwellian EEDF of $T_e = 4$ eV (section 5.2).

An important result of this study is the characterization of the time-varying EEDF, which is directly linked to the plasma light emission. Its impact should be further investigated, coupling the simulation results with a collision-radiative model taking into account the EEDF features (e.g. [55]). In the present work we have not discussed details of the neutral population (atomic and vibrational density/temperatures). Their dynamics require a longer simulation time ($\approx$ 25–30 µs in the Linac4 ion source case), and this will be the object of a future publication. Furthermore, we plan to extend the model to address non-axisymmetric features, such as the external magnetic cusp and filter field.

In the specific case of the Linac4 H^- ion source, the present results represent crucial input for beam formation simulations [56,57], that rely on the specifications of the plasma parameters in the extraction region (conical region at $z > 116$ mm). This is particularly important since spatially resolved measurements are difficult to achieve in this region due to space limitations. Coupling between these simulations, beam formation simulations and beam measurements could indicate possible improvements to the plasma generator configuration as well as a better understanding of the beam extraction physics.

7. Conclusions and outlook

We have presented the algorithms and the implementation of a fully-implicit PIC-MCC code, NINJA, for the simulation of inductively coupled plasmas. The model solves self-consistently the coupling between the electromagnetic field generated by the RF coil and the plasma dynamics, composed of the kinetic description of charged and neutral particles together with the collision processes between them. The governing equations are solved with a kinetic enslaved Jacobian-Free Newton Krylov method, in which a preconditioner is supplied to enhance the performance.

A key feature of the method is the possibility of performing kinetic simulations of high density, low temperature plasmas with cell sizes $\gg \lambda_{De}$ and time step in excess of the Courant–Friedrichs–Lewy condition whilst preserving the conservation of the total energy. The application to the CERN Linac4 H^- ion source shows that with a cell size sufficient to resolve the plasma skin depth, an accurate representation of the plasma parameters is achieved. This is confirmed by agreement between simulations and optical emission spectroscopy measurements on the range of density and temperatures.

Simulation results show that the EEDF varies in time during one RF cycle, with a deviation of the high-energy tail from a Maxwellian distribution. Coupling with a collision-radiative model taking into account the simulated EEDF will allow to investigate its impact on the light emission and provide refined comparisons to optical emission spectroscopy measurements. The plasma parameters and neutral fluxes will be simulated for variable hydrogen densities, RF current and position of the RF coil to define the input for the optimization process of the Linac4 H^- ion source. This will include coupling of the present simulation results to beam formation and extraction software-packages [56,58], capable of simulating effective beam emittance and intensity.

We have detailed the algorithms used for an ICP in cylindrical geometry with a solenoid RF coil, using hydrogen as the discharge gas. The model can easily be adapted to other gases provided the availability of collision cross-sections as well as to the simulations of ICPs in planar configuration.

References

[1] J. Hopwood, Review of inductively coupled plasmas for plasma processing, Plasma Sources Sci. Technol. 1 (2) (1992) 109, http://stacks.iop.org/0963-0252/1/i=2/a=006.

[2] M. Laroussi, Low temperature plasma-based sterilization: overview and state-of-the-art, Plasma Process. Polym. 2 (5) (2005) 391–400, http://dx.doi.org/10.1002/ppap.200400078.

[3] J. Lettry, D. Aguglia, J. Alessi, P. Andersson, S. Bertolo, S. Briefi, A. Butterworth, Y. Coutron, A. Dallocchio, N. David, E. Chaudet, D. Faircloth, U. Fantz, D.A. Fink, M. Garlasche, A. Grudiev, R. Guida, J. Hansen, M. Haase, A. Hatayama, A. Jones, I. Koszar, J.-B. Lallement, A.M. Lombardi, C. Machado, C. Mastrostefano, S. Mathot, S. Mattei, P. Moyret, D. Nisbet, K. Nishida, M. O'Neil, M. Paoluzzi, R. Scrivens, T. Shibata, D. Steyaert, N. Thaus, G. Voulgarakis, Linac4 H^- ion source, Rev. Sci. Instrum. 87 (2016) 02B139, http://dx.doi.org/10.1063/1.4936120.

[4] U. Fantz, B. Heinemann, D. Wünderlich, R. Riedl, W. Kraus, R. Nocentini, F. Bonomo, Towards 20 A negative hydrogen ion beams for up to 1 h: achievements of the ELISE test facility (invited), Rev. Sci. Instrum. 87 (2016) 02B307, http://dx.doi.org/10.1063/1.4932560.

[5] H. Singh, D.B. Graves, Measurements of the electron energy distribution function in molecular gases in an inductively coupled plasma, J. Appl. Phys. 87 (9) (2000) 4098–4106, http://dx.doi.org/10.1063/1.373036.

[6] V.I. Kolobov, D.P. Lymberopoulos, D.J. Economou, Electron kinetics and non-joule heating in near-collisionless inductively coupled plasmas, Phys. Rev. E 55 (1997) 3408–3422, http://dx.doi.org/10.1103/PhysRevE.55.3408.

[7] U. Kortshagen, I. Pukropski, L.D. Tsendin, Experimental investigation and fast two-dimensional self-consistent kinetic modeling of a low-pressure inductively coupled rf discharge, Phys. Rev. E 51 (1995) 6063–6078, http://dx.doi.org/10.1103/PhysRevE.51.6063.

[8] H.-C. Lee, M.-H. Lee, C.-W. Chung, Experimental observation of the transition from nonlocal to local electron kinetics in inductively coupled plasmas, Appl. Phys. Lett. 96 (2010) 041503, http://dx.doi.org/10.1063/1.3291038.

[9] R.A. Stewart, P. Vitello, D.B. Graves, Two-dimensional fluid model of high density inductively coupled plasma sources, J. Vac. Sci. Technol., B 12 (1) (1994) 478–485, http://dx.doi.org/10.1116/1.587102.

[10] J.D. Bukowski, D.B. Graves, P. Vitello, Two-dimensional fluid model of an inductively coupled plasma with comparison to experimental spatial profiles, J. Appl. Phys. 80 (5) (1996) 2614–2623, http://dx.doi.org/10.1063/1.363169.

[11] H.C. Kim, F. Iza, S.S. Yang, M. Radmilović-Radjenović, J.K. Lee, Particle and fluid simulations of low-temperature plasma discharges: benchmarks and kinetic effects, J. Phys. D, Appl. Phys. 38 (19) (2005) R283, http://stacks.iop.org/0022-3727/38/i=19/a=R01.

[12] P.L.G. Ventzek, T.J. Sommerer, R.J. Hoekstra, M.J. Kushner, Two-dimensional hybrid model of inductively coupled plasma sources for etching, Appl. Phys. Lett. 63 (5) (1993) 605–607, http://dx.doi.org/10.1063/1.109963.

[13] K. Nishida, S. Mattei, S. Mochizuki, J. Lettry, A. Hatayama, Kinetic modeling of E-to-H mode transition in inductively coupled hydrogen plasmas, J. Appl. Phys. 119 (2016) 233302, http://dx.doi.org/10.1063/1.4953647.

[14] M. Ohta, S. Mattei, M. Yasumoto, A. Hatayama, J. Lettry, Numerical study of the inductive plasma coupling to ramp up the plasma density for the Linac4 H^- ion source, Rev. Sci. Instrum. 85 (2) (2014) 02B113, http://dx.doi.org/10.1063/1.4833920.

[15] S. Mattei, K. Nishida, S. Mochizuki, A. Grudiev, J. Lettry, M.Q. Tran, A. Hatayama, Kinetic simulations and photometry measurements of the E-H transition in cylindrical inductively coupled plasmas, Plasma Sources Sci. Technol. 25 (6) (2016) 065001, http://stacks.iop.org/0963-0252/25/i=6/a=065001.

[16] C.K. Birdsall, A.B. Langdon, Plasma Physics via Computer Simulation, CRC Press, 2004.

[17] A. Langdon, Effects of the spatial grid in simulation plasmas, J. Comput. Phys. 6 (2) (1970) 247–267, http://dx.doi.org/10.1016/0021-9991(70)90024-0.

[18] R.J. Mason, Implicit moment particle simulation of plasmas, J. Comput. Phys. 41 (2) (1981) 233–244, http://dx.doi.org/10.1016/0021-9991(81)90094-2.

[19] J. Denavit, Time-filtering particle simulations with $\omega_{pe}\Delta t \gg 1$, J. Comput. Phys. 42 (2) (1981) 337–366, http://dx.doi.org/10.1016/0021-9991(81)90249-7.

[20] A. Friedman, A. Langdon, B. Cohen, A direct method for implicit particle-in-cell simulation, Comments Plasma Phys. Control. Fusion 6 (6) (1981) 225–236.

[21] G. Chen, L. Chacón, D. Barnes, An energy- and charge-conserving, implicit, electrostatic particle-in-cell algorithm, J. Comput. Phys. 230 (18) (2011) 7018–7036, http://dx.doi.org/10.1016/j.jcp.2011.05.031.

[22] S. Markidis, G. Lapenta, The energy conserving particle-in-cell method, J. Comput. Phys. 230 (18) (2011) 7037–7052, http://dx.doi.org/10.1016/j.jcp.2011.05.033.

[23] P. Chabert, N. Braithwaite, Physics of Radio-Frequency Plasmas, Cambridge University Press, 2011.

[24] K. Yee, Numerical solution of initial boundary value problems involving Maxwell's equations in isotropic media, IEEE Trans. Antennas Propag. 14 (3) (1966) 302–307, http://dx.doi.org/10.1109/TAP.1966.1138693.
[25] J. Brackbill, D. Forslund, An implicit method for electromagnetic plasma simulation in two dimensions, J. Comput. Phys. 46 (2) (1982) 271–308, http://dx.doi.org/10.1016/0021-9991(82)90016-X.
[26] J. Verboncoeur, Symmetric spline weighting for charge and current density in particle simulation, J. Comput. Phys. 174 (1) (2001) 421–427, http://dx.doi.org/10.1006/jcph.2001.6923.
[27] G. Mur, Absorbing boundary conditions for the finite-difference approximation of the time-domain electromagnetic-field equations, IEEE Trans. Electromagn. Compat. EMC-23 (4) (1981) 377–382, http://dx.doi.org/10.1109/TEMC.1981.303970.
[28] A. Bayliss, E. Turkel, Radiation boundary conditions for wave-like equations, Commun. Pure Appl. Math. 33 (6) (1980) 707–725.
[29] W.T. Taitano, Development of a Jacobian-Free Newton–Krylov Method with Kinetic Enslavement to Implicitly Solve Vlasov–Poisson System in Plasma Physics, Master's thesis, University of Idaho, 2010.
[30] M. Pernice, H.F. Walker, Nitsol: a Newton iterative solver for nonlinear systems, SIAM J. Sci. Comput. 19 (1) (1998) 302–318.
[31] J. Brackbill, B. Cohen, Simulation of low-frequency, electromagnetic phenomena in plasma, in: Multiple Time Scales, Academic Press, Inc., 1985, pp. 271–310.
[32] J.P. Boris, Relativistic plasma simulation-optimization of a hybrid code, in: Proceeding of Fourth Conference on Numerical Simulations of Plasmas.
[33] J.M. Wallace, J.U. Brackbill, D.W. Forslund, An implicit moment electromagnetic plasma simulation in cylindrical coordinates, J. Comput. Phys. 63 (2) (1986) 434–457.
[34] K. Nanbu, Probability theory of electron-molecule, ion-molecule, molecule-molecule, and Coulomb collisions for particle modeling of materials processing plasmas and gases, IEEE Trans. Plasma Sci. 28 (3) (2000) 971–990.
[35] T. Takizuka, H. Abe, A binary collision model for plasma simulation with a particle code, J. Comput. Phys. 25 (3) (1977) 205–219, http://dx.doi.org/10.1016/0021-9991(77)90099-7.
[36] S. Mochizuki, S. Mattei, T. Shibata, K. Nishida, A. Hatayama, J. Lettry, Initial results of a full kinetic simulation of RF H^- source including Coulomb collision process, in: Fourth International Symposium on Negative Ions Beams and Sources, NIBS 2014, vol. 1655, AIP Publishing, 2015, 020016.
[37] R.K. Janev, W.D. Langer, K. Evans Jr., E. Douglass Jr., Elementary Processes in Hydrogen-Helium Plasmas: Cross Sections and Reaction Rate Coefficients, vol. 4, Springer-Verlag, Berlin, Heidelberg, 1987.
[38] S. Buckman, Y. Itikawa, Interactions of Photons and Electrons with Atoms, Springer, 2000.
[39] R.K. Janev, D. Reiter, U. Samm, Collision processes in low-temperature hydrogen plasmas, Juel-Report 4105 (2003).
[40] S. Buckman, et al., Interactions of Photons and Electrons with Molecules, Springer-Verlag, 2003.
[41] P.T. Greenland, D. Reiter, F. Jülich, The Role of Molecular Hydrogen in Plasma Recombination, Forschungszentrum Jülich, 1996.
[42] J. Hiskes, Cross sections for the vibrational excitation of the $H_2\ X^1\Sigma_g^+(v)$ levels generated by electron collisional excitation of the higher singlet states, J. Appl. Phys. 70 (7) (1991) 3409–3417.
[43] P. Krstic, D. Schultz, Elastic and related transport cross sections for collisions among isotopomers of $H^+ + H$, $H^+ + H_2$, $H^+ + He$, $H + H$ and $H + H_2$, Plasma-Mater. Data Fusion 8 (1).
[44] A.V. Phelps, Cross sections and swarm coefficients for H^+, H_2^+, H_3^+, H, H_2, and H^- in H_2 for energies from 0.1 eV to 10 keV, J. Phys. Chem. Ref. Data 19 (3) (1990) 653–675, http://dx.doi.org/10.1063/1.555858.
[45] A. Aanesland, L. Liard, G. Leray, J. Jolly, P. Chabert, Direct measurements of neutral density depletion by two-photon absorption laser-induced fluorescence spectroscopy, Appl. Phys. Lett. 91 (2007) 121502, http://dx.doi.org/10.1063/1.2786601.
[46] G. Lapenta, Particle rezoning for multidimensional kinetic particle-in-cell simulations, J. Comput. Phys. 181 (1) (2002) 317–337, http://dx.doi.org/10.1006/jcph.2002.7126.
[47] Y. Saad, Sparsekit: A Basic Tool Kit for Sparse Matrix Computations, Tech. rep., University of Minnesota, Computer Science Department, June 1994.
[48] M.A. Lieberman, A.J. Lichtenberg, Principles of Plasma Discharges and Materials Processing, John Wiley & Sons, 2005.
[49] S. Briefi, S. Mattei, J. Lettry, U. Fantz, Influence of the cusp field on the plasma parameters of the Linac4 H^- ion source, in: Proceedings of 5th NIBS Conference, Oxford, UK, 2016.
[50] Y.P. Raizer, J.E. Allen, Gas Discharge Physics, vol. 2, Springer, Berlin, 1997.
[51] S. Mochizuki, S. Mattei, K. Nishida, A. Hatayama, J. Lettry, Analysis of electron energy distribution function in the Linac4 H^- source, Rev. Sci. Instrum. 87 (2016) 02B108, http://dx.doi.org/10.1063/1.4932322.
[52] M.M. Turner, Kinetic properties of particle-in-cell simulations compromised by Monte Carlo collisions, Phys. Plasmas 13 (3) (2006) 033506, http://dx.doi.org/10.1063/1.2169752.
[53] J. Brackbill, On energy and momentum conservation in particle-in-cell plasma simulation, J. Comput. Phys. 317 (2016) 405–427, http://dx.doi.org/10.1016/j.jcp.2016.04.050.
[54] G. Chen, L. Chacón, C. Leibs, D. Knoll, W. Taitano, Fluid preconditioning for Newton–Krylov-based, fully implicit, electrostatic particle-in-cell simulations, J. Comput. Phys. 258 (2014) 555–567, http://dx.doi.org/10.1016/j.jcp.2013.10.052.
[55] T. Shibata, M. Kashiwagi, A. Hatayama, K. Sawada, T. Inoue, M. Hanada, Numerical study of the H^0 atomic density and the balmer line intensity profiles in a hydrogen negative ion source with the effect of non-equilibrium electron energy distribution function, J. Plasma Fusion Res. 9 (2014) 1401011, http://dx.doi.org/10.1585/pfr.9.1401011.
[56] S. Mochalskyy, J. Lettry, T. Minea, Beam formation in CERNs cesiated surfaces and volume H^- ion sources, New J. Phys. 18 (8) (2016) 085011, http://stacks.iop.org/1367-2630/18/i=8/a=085011.
[57] S. Abe, S. Nishioka, S. Mattei, A. Hatayama, J. Lettry, Effect of the puller-electrode voltage on the extraction in Linac4 negative ion source, in: Proceedings of 5th NIBS Conference, Oxford, UK, 2016.
[58] S. Nishioka, I. Goto, K. Miyamoto, A. Hatayama, A. Fukano, Study of ion-ion plasma formation in negative ion sources by a three-dimensional in real space and three-dimensional in velocity space particle in cell model, J. Appl. Phys. 119 (2) (2016) 023302, http://dx.doi.org/10.1063/1.4939467.